Journal of Magnetism and Magnetic Materials 608 (2024) 172447

Contents lists available at ScienceDirect

Journal of Magnetism and Magnetic Materials

journal homepage: www.elsevier.com/locate/jmmm

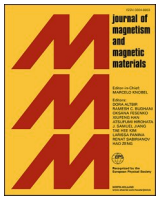

Citrate stabilized maghemite hydrosol with controllable MRI contrast: Key role of nanoparticle size

Ekaterina O. Moiseeva [a], Sergei V. German [a], Aleksei S. Komlev [b], Vyacheslav S. Rusakov [b], Viktor V. Zuev [c], Olga S. Pavlova [d], Alexander M. Perepukhov [e], Artem O. Dmitrienko [f], Konstantin I. Maslakov [f], Olga Y. Griaznova [a,g], Alexander V. Finko [f], Antonina I. Dadadzhanova [h], Vasiliy S. Chernyshev [i], Anna O. Orlova [h], Dmitry A. Gorin [a,*]

[a] Center for Photonic Science and Engineering, Skolkovo Institute of Science and Technology, 143026 Moscow, Russia
[b] Faculty of Physics, M.V. Lomonosov Moscow State University, 119991 Moscow, Russia
[c] Department of Radiation Diagnostics, Sechenov First Moscow State Medical University, 119991 Moscow, Russia
[d] Faculty of Fundamental Medicine, Lomonosov Moscow State University, 119991 Moscow, Russia
[e] Moscow Institute of Physics and Technology, Dolgoprudny 141701, Russia
[f] Faculty of Chemistry, Lomonosov Moscow State University, 119991 Moscow, Russia
[g] Shemyakin-Ovchinnikov Institute of Bioorganic Chemistry of the Russian Academy of Sciences, 117997 Moscow, Russia
[h] International Research and Education Centre for Physics of Nanostructures, ITMO University, 197101 Saint Petersburg, Russia
[i] National Medical Research Center for Obstetrics, Gynecology and Perinatology Named After Academician V.I. Kulakov, 117997 Moscow, Russia

ARTICLE INFO

Keywords:
Superparamagnetic nanoparticles
Maghemite hydrosol
Magnetic resonance imaging
T1 contrast agents
Nanoparticle size effect

ABSTRACT

In this study, we have synthetized a series of citric acid stabilized superparamagnetic iron oxide nanoparticles (CA-SPIONs) with different core sizes in an automated chemical reactor with high repeatability of the nanoparticle size and chemical composition. The prepared CA-SPIONs are highly crystalline spherical-shaped particles with the diameters of 3.5 ± 0.7, 6 ± 1, 9 ± 1, and 12 ± 2 nm. The valent state of iron oxide was determined by a combination of X-ray photoelectron spectroscopy, UV–Vis spectroscopy, and Mössbauer studies, which confirmed predominantly maghemite formation. Under normal conditions, these nanoparticles exhibit no coercive force and no hysteresis, while saturation magnetization increases from 2 to 61 emu/g along with the increasing core size. Both longitudinal (r_1) and transverse (r_2) relaxivities of maghemite hydrosols with different nanoparticle sizes were measured and compared with the same data for the commercial Gd-complex (Gadovist). Magnetic circular dichroism spectroscopy indicated that aggregation occurs in magnetic field, but 9 nm samples slightly aggregate in the fields above 1.0 T, whereas 3.5 nm colloids are stable and do not exhibit aggregation behavior even at 1.5 T. The obtained series were examined in phantom test in clinical 1.5 T MRI scanner, which showed that increasing the particle core size resulted in an enhanced T_2 contrast, while T_1 contrast declined. Finally, the smallest CA-SPION colloid nanoparticles with the size of 3.5 nm exhibited significant T_1 contrast enhancement, comparable with the commercial Gd-complex in water and human plasma as well. The maghemite hydrosol formed by nanoparticles with 3.5 nm size thus has a promising future as a T_1 MRI contrast agent.

1. Introduction

The number of applications of magnetic resonance imaging (MRI) has increased dramatically over the past decade [1]. This imaging modality is currently the most commonly used cross-sectional imaging technique for diagnostics of brain, spine, and musculoskeletal diseases due to its non-invasive nature and multidimensional tomographic capabilities [2]. The majority of MRI contrast agents are paramagnetic complexes of Gd^{3+} ions. As positive contrast agents, Gd^{3+} chelates amplify the signal in T_1-weighted images (T_1-WIs), but have a less pronounced effect in T_2-weighted images (T_2-WIs) [3]. The high magnetic susceptibility of the typical T_2 contrast agents, which are superparamagnetic iron oxide nanoparticles (SPIONs) [4,5], can distort the magnetic fields of the neighboring normal tissues. The distortion results

* Corresponding authors.
E-mail address: d.gorin@skoltech.ru (D.A. Gorin).

https://doi.org/10.1016/j.jmmm.2024.172447
Received 2 June 2024; Received in revised form 1 August 2024; Accepted 20 August 2024
Available online 20 August 2024

in dark images appearing around the lesions without a background, which in turn contributes to artefacts during scanning [6]. Additionally, the occurrence of magnetic susceptibility artifacts at the border of tissues is more common for SPIONs than for Gd-complexes, since iron oxide nanoparticles can accumulate in normal tissues. Consequently, SPIONs are used less often than gadolinium-based contrast agents.

However, after decades of successful application of Gd complexes in MRI, in 2007 the European Medicines Agency (EMA) and in 2010 the U. S. Food and Drug Administration (FDA) associated gadolinium chelates with a devastating and potentially fatal condition called nephrogenic systemic fibrosis (NSF) [7]. Although severe side effects leading to NSF are rare (less than 0.05 %), the risk for people with kidney problems is significant [8]. Later in 2017 [9], the FDA issued a new warning that gadolinium can stay in the body for months or years after MRI scans. A condition called "gadolinium retention" occurs when it builds up in the bones, brain, and kidney, and it does not depend on kidney function. The safety concerns about the gadolinium-based contrast agents have therefore necessitated the quest for T_1 contrast alternatives.

The ultra-small SPIONs with sizes less than 10 nm also possess good T_1 relaxivity, [10–13], making them suitable for positive MR contrast. Unlike gadolinium, iron is a non-toxic biogenic element. The expected lethal iron dose for an adult (~70 kg) is 2–4 g of iron [14]. In the liver SPIONs become metabolized into a soluble and inactive form of iron, which is incorporated into the normal iron pool, including heme proteins such as ferritin and hemoglobin [15,16]. Several SPION formulations were approved for clinical application as MRI contrast agents by the EMA and FDA. Unfortunately, to date, most of them have been withdrawn from the market [5,17] after disputes about their demand for cancer diagnostics [18]. Ferumoxytol (Feraheme®, Covis Pharma) is the only SPION formulated product that is still in clinical practice [19]. The drug was initially approved for treating iron-deficiency anemia, but it is also used as an off-label contrast agent for MRI [20,21].

For a T_1 agent to be effective, it should show a high value for r_1 relaxivity and a low r_2/r_1 ratio at least less than 2 [22]. As most of the available iron oxide nanoparticles have extremely high transverse relaxivity (r_2), they are not suitable for T_1 contrast due to their high r_2/r_1 ratio, which brings about a strong T_2 effect and prevents T_1 enhancement. The saturation magnetization (M_s) can be reduced by decreasing the size of SPIONs and applying an appropriate coating [23,24]. Over the last decade, several research groups developed ultra-small SPIONs with a high r_1 relaxivity above10 $L{\cdot}mmol^{-1}{\cdot}s^{-1}$ and r_2/r_1 ratio around 2 [12,25–29]. Generally, most of these particles consist of a maghemite core less than 6 nm in diameter and a hydrodynamic size not exceeding tens of nm. Unlike magnetite (Fe_3O_4), maghemite (γ-Fe_2O_3) is more stable, non-toxic and has less effect on r_2 relaxation [23,30–32].

Iron oxide nanoparticles stabilized in citric acid exhibit a low toxicity profile due to their biocompatibility [15]. As citric acid is involved in the Krebs cycle, it is not a xenobiotic and can be easily metabolized by humans. The citric acid coated SPIONs also known as VSOP were designed for MR angiography and blood pool imaging by Ferropharm (Germany). In phase I and II clinical trials, they demonstrated a favorable safety profile without any allergic reactions [33,34], but these studies were terminated and eventually VSOP did not receive the regulatory approval. Nevertheless, these SPIONs showed remarkable T_1 contrast enhancement almost equal to FDA-approved Gd chelate and even greater potential including first-pass MRA or detection of CNS disorders [35,36].

Here, we present an automated preparation procedure of the electrostatically stabilized water-soluble maghemite MRI contrast agent. We fabricate a series of citric acid stabilized iron oxide nanoparticles (CA-SPIONs) with different core sizes ranging from 3.5 to 12 nm and polydispersity index less than 0.2. Its low-cost preparation method, long-term stability during storage, absence of aggregation under the applied magnetic fields up to clinical 1.5 T, and ability to create an enhanced positive contrast in biological fluids make these CA-SPIONs a highly promising MRI contrast agent as well as a viable alternative to gadolinium-based contrasts.

2. Experimental section

Materials. Iron (III) chloride hexahydrate (99.8 %, Sigma-Aldrich), sodium hydroxide (99.8 %, Fluka), ammonium thiocyanate (99 %, Sigma-Aldrich), ammonium persulfate (98 %, Merck) and citric acid (99.8 %, Sigma-Aldrich), *o*-phenanthroline monohydrate (97 %, Lenreactive, Russia), gadobutrol (Gadovist, Bayer Schering Pharma) were used as received. The iron (II) chloride tetrahydrate (99.8 %, Sigma-Aldrich) was recrystallized before use. All solutions were made from deionized water (Milli-Q, pH=6.2, 18.2 MΩ·cm, Millipore, USA).

Synthesis of citric acid stabilized iron oxide nanoparticles (CA-SPIONs). Electrostatically stabilized SPIONs were synthesized by using a modified Massart coprecipitation procedure [37] in the chemical reactor TetraQuant CR-1 (TetraQuant LLC, Russia). For a typical synthesis, 50 mL of solution containing a mixture of 0.4 mol/L iron (III) chloride hexahydrate and 0.2 mol/L iron (II) chloride tetrahydrate salts was injected into 300 mL of 0.3 mol/L sodium hydroxide solution at 40 °C under vigorous stirring. Following black precipitate formation, the suspension was additionally mixed during 1, 5 and 15 min to prepare 3.5 (S1), 6 (S2) and 9 nm (S3) SPION particles, respectively. Then, 50 mL of 1.5 mol/L citric acid water solution was added to the suspension under intense stirring for 5 more minutes. After the reaction was complete the suspension was transferred to a dialysis membrane (MD 44, MW 14000) and placed in 3 L of deionized water. The magnetic colloid was dialyzed for 4 days with slow stirring under room temperature. To prepare 12 nm particles (S4) citric acid was added to the reaction mixture after 15 min, and ammonia was used as a base instead of sodium hydroxide.

2.1. Characterization of maghemite hydrosol and nanoparticles

X-ray powder diffraction (XRD) analysis of nanoparticles was performed using a Rigaku Miniflex 600 diffractometer (CuKα radiation, Kβ filter, and D/teX Ultra detector). Attenuated total reflectance Fourier transform infrared spectroscopy (ATR-FT-IR) was conducted using an IR 200 Thermo Scientific Nicolet iS5 FT-IR spectrometer with a spectral resolution (Δλ) of 4 cm^{-1}.

Transmission Mössbauer spectra of nanoparticles between 7 and 298 K were recorded on a constant-acceleration spectrometer MS-1104Em equipped with a ^{57}Co source in a Rh matrix with an activity of ~ 20 mCi and a closed cycle He cryogenerator SHI-850H-5. The spectrometer was calibrated against a reference sample of α-Fe at room temperature. The spectra were fitted using the SpectrRelax program [38]. For XRD, IR and Mössbauer experiments the stock aqueous iron oxide hydrosol was placed in a Schlenk tube and heated at 60 °C in intensive argon flow to water evaporation. The resulting precipitate was further dried under vacuum for 12 h.

High resolution transmission electron microscopy (HR-TEM) images and energy dispersive X-ray (EDX) spectra of nanoparticles were recorded with a FEI Titan G3 microscope. For TEM analysis, the samples were diluted and precipitated on carbon-coated copper grids. A minimum of 300 particles were analyzed using ImageJ for each sample.

X-ray photoelectron spectroscopy (XPS) analysis was carried out on an Axis Ultra DLD spectrometer (Kratos Analytical, UK) with the monochromatic Al Kα X-ray source (1486.7 eV, 150 W) under ultra-high vacuum conditions (10^{-9} mbar). Pass energies of 160 and 40 eV were used for survey spectra and high-resolution scans.

Raman spectra of nanoparticles were obtained by Raman spectrometer LabRAM HR Evolution (HORIBA France SAS, Longjumeau, France), equipped with a diffraction grating 600 lines/mm, objective Olympus MPlan 50x, 633 nm laser at 12 mW power, and 2 s exposure time; 5 accumulations were used. For XPS and Raman spectra the drops of aqueous colloids were deposited on a silicon wafer and dried under argon flow.

Hydrodynamic diameters and Zeta potential of nanoparticles

were measured by the dynamic light scattering (DLS) and electrophoretic light scattering (ELS) respectively using Malvern Nano ZS Zetasizer (Malvern Panalytical, United Kingdom). Deionized water was used as a solvent and the maghemite hydrosol contained 2 mmol/L of iron for each sample.

The field dependences of the magnetization of nanoparticles were measured using a vibrational sample magnetometer (Lake Shore 7407). The measured saturation magnetization (emu/g) is given per unit of mass of citric acid stabilized iron oxide nanoparticles. All samples for magnetization experiments were heated at 60 °C in argon flow to water evaporation.

Magnetic circular dichroism (MCD) spectra of maghemite hydrosol were measured on a JASCO J-1500 circular dichroism spectrometer at wavelengths of 200–800 nm with a magnetic field from 0 to ± 1.5 T. Deionized water was used as a solvent. The concentration was 0.02 mmol/L of iron for both S1 (3.5 nm) and S3 (9 nm) samples.

Iron concentration analysis in maghemite hydrosol was evaluated by the spectrophotometric and inductively coupled plasma mass spectrometry (ICP-MS) methods independently. To determine the concentration of ferrous and ferric iron in aqueous colloid, the CA-SIONs were dissolved in concentrated hydrochloric acid in argon atmosphere. The UV–Vis absorption spectra of ferrous *o*-phenanthroline and ferric thiocyanate complexes were measured using Tecan Infinite M200 Microplate Reader. The standard error was estimated from five independent measurements of the same sample. For the ICP-MS measurements, the CA-SPIONs were dissolved in concentrated nitric acid, then total iron concentration in solution was measured using NexION 2000 mass spectrometer (PerkinElmer, USA), utilizing a ^{57}Fe peak for the analysis.

Relaxometry. MR T_1 and T_2 relaxation time constants were measured with TD-NMR Spectrometer Bruker Minispec at 20 MHz (0.47 T), and a temperature of 38 °C. For relaxivity measurements, the stock aqueous colloid of CA-SPION and clinically approved Gd-based contrast agent Gadovist (Gd) were gradually diluted in deionized water to prepare solutions with the concentrations of 0.16 – 10 mmol/L for S1-S3 and of 0.03 – 1.0 mmol/L for S4 samples, and of 0.2 – 6.4 mmol/L for Gd.

MR imaging. MRI of water and human plasma phantoms was performed using Siemens Magnetom Aera 1.5 T clinical MRI scanner. We obtained T_1 and T_2-weighted images using T_1 and T_2 spin-echo (SE) sequences. The scanning parameters were echo time (TE) 9.2 ms and repetition time (TR) 772 ms for T_1, and TE=84 ms and TR=3500 ms for T_2. These parameters remained unchanged for all the samples within one visualization mode. The phantoms with different concentration of iron or gadolinium were prepared in 2-mL polymeric centrifuge tubes by diluting the contrast agent in deionized water or human plasma. During MRI tests the tubes filled with the corresponding CA-SPION hydrosols or Gd solutions were fixed on the bottom of a plastic container filled with deionized water as a reference. The human plasma was obtained from blood samples collected with written informed consent from healthy donors with permission from the local Ethics Committee of the V.I. Kulakov National Medical Research Center for Obstetrics, Gynecology, and Perinatology (Protocol № 8 approved on September 3, 2020). Cells were removed by centrifugation for 10 min at 1000 × g and 4 °C followed by centrifugation at 2000 × g and 4 °C to remove platelets and obtain plasma. Plasma samples were aliquoted and stored at –20 °C until use. Additional relaxation rates at high field 7 T MRI were performed on a Bruker BioSpec 70/30 USR scanner. T_1 and T_2 relaxation times were measured for 1 % agarose solutions with different contrast agent concentrations, and corresponding relaxivities for SPIONs and Gd-based contrast agents were calculated (see details in supplementary material).

3. Results and discussion

3.1. Synthesis and characterization of CA-SPIONs

Numerous research papers have investigated the preparation routes of iron oxide nanoparticles, but the most appropriate method for achieving the desired properties is still debated. Although in recent years the most common thermal decomposition methods have allowed for synthesizing the uniform iron oxide nanoparticles ranging in size from a few to tens of nanometers with high crystallinity [39], we still believe the conventional coprecipitation methods are more applicable for preparing the MRI contrast agents. In our experiments the alkaline coprecipitation of ferric and ferrous iron salts in aqueous solutions in an automatic chemical reactor produces fine water-soluble SPIONs with high yield. The core size of the obtained CA-SPIONs can be controlled from 3.5 to 12 nm by simply varying and fine-tuning the reaction conditions. This method is inexpensive, environmentally friendly, easy to scale-up and highly repeatable [40].

TEM images revealed the well-defined spherical nanoparticles without aggregates and extremely small or large cores in all samples (Fig. 1a-d). The average diameters for samples S1, S2 and S3 precipitated with sodium hydroxide were 3.5 ± 0.7, 6 ± 1, and 9 ± 1 nm respectively (Fig. 1e). These particles were obtained with the reaction time ranging from 1 to 15 min. We also tried to extend the reaction time, but this did not result in any significant core size growth. Instead, a large number of particles of arbitrary shape with a broader size distribution were formed (Fig. S1, supplementary material). The size of iron oxide particles prepared by the iron salt coprecipitation reaction was earlier reported to be strongly affected by the base used [41], so to obtain the particles with diameters greater than 10 nm, we replaced the base with ammonia. This can be explained by the dual role of ammonia. First, when it is used as a base, a buffer medium with a constant pH of 9–10 is formed, which is optimal for the secondary particle growth by Ostwald ripening of iron oxide cores [42]. Second, the negative charge caused by the adsorption of hydroxyl ions on a surface can be stabilized with an ammonium cation, preventing nanoparticles from aggregation. The average diameter of the nanoparticles obtained in ammonia (S4) was found to be 12 ± 1 nm. The polydispersity index, which measures the relative standard deviations among particle sizes, was around 0.2 for all samples.

The EDX spectroscopy analysis shows that the nanoparticles contain iron and oxygen. All samples have almost identical spectra, the EDX spectrum for sample S2 (6 nm) is given in supplementary material (Fig. S2). The spectrum shows that even the trace amounts of sodium, nitrogen, and chlorine are absent in the sample. It confirms that the CA-SPION aqueous colloid is devoid of any inorganic ions after dialysis.

Hydrophilic water-soluble nanoparticles are preferred over the hydrophobic ones derived from solvothermal reactions, because they do not require any additional procedures typically involved in capping with amphiphilic agents such as poly(ethylene glycol)-derivatives to transfer these nanoparticles into the aqueous phase [12]. As a result, the synthesis is complicated and the contrast properties and biodistribution of these nanoparticles can be significantly affected. A relatively high polydispersity index (PDI) is considered to be the major disadvantage of the coprecipitation reaction. Indeed, it is typical of SPIONs obtained in thermal decomposition reactions [43], to prepare monodisperse nanoparticles with PDI<0.05. Nevertheless, PDI up to 0.2–0.3 is acceptable for MRI applications and does not negatively affect MRI performance. For example, iron oxide nanoparticles with 3 nm core and 4.4 nm hydrodynamic diameter obtained via thermal decomposition method exhibit $r_1 = 1.5$ and $r_2 = 17$ L·mmol^{-1}·s^{-1} ($r_2/r_1 = 11$), [25] while our CA-SPIONs with 3.5 nm core and 6 nm hydrodynamic diameter reveal $r_1 = 1.41$ and $r_2 = 14.2$ L·mmol^{-1}·s^{-1} ($r_2/r_1 = 10$) at 7 T (see detailed experimental description in the supplementary material). The inhomogeneity of the core size can lead to T_2 contrast enhancement [44], but it seems that the non-uniformity of the particles is not critical, since CA-SPIONs obtained via coprecipitation display almost the same r_2/r_1 when compared to the monodispersed particles prepared by thermal decomposition.

X-ray powder diffraction (XRD) analysis was performed for all the samples, which differed in the average diameters (Fig. 2a). The XRD analysis does not always allow distinguishing between magnetite,

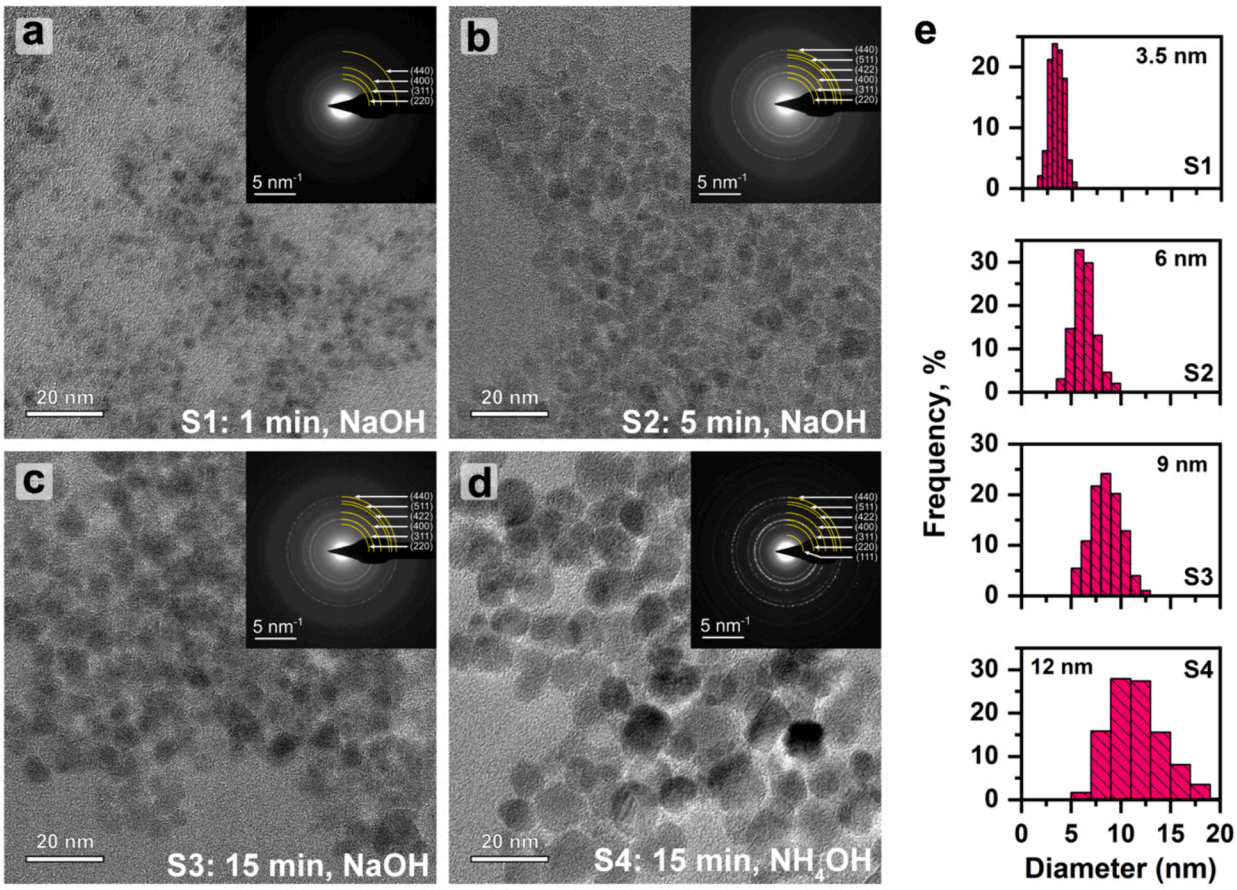

Fig. 1. Morphology and size distribution of the CA-SPIONs obtained with different reaction conditions. TEM images of a) 3.5 nm (S1), b) 6 nm (S2), c) 9 nm (S3) and d) 12 nm (S4) samples of CA-SPIONs; Inserts: selected area electron diffraction pattern; e) histograms of the core diameters measured from TEM images.

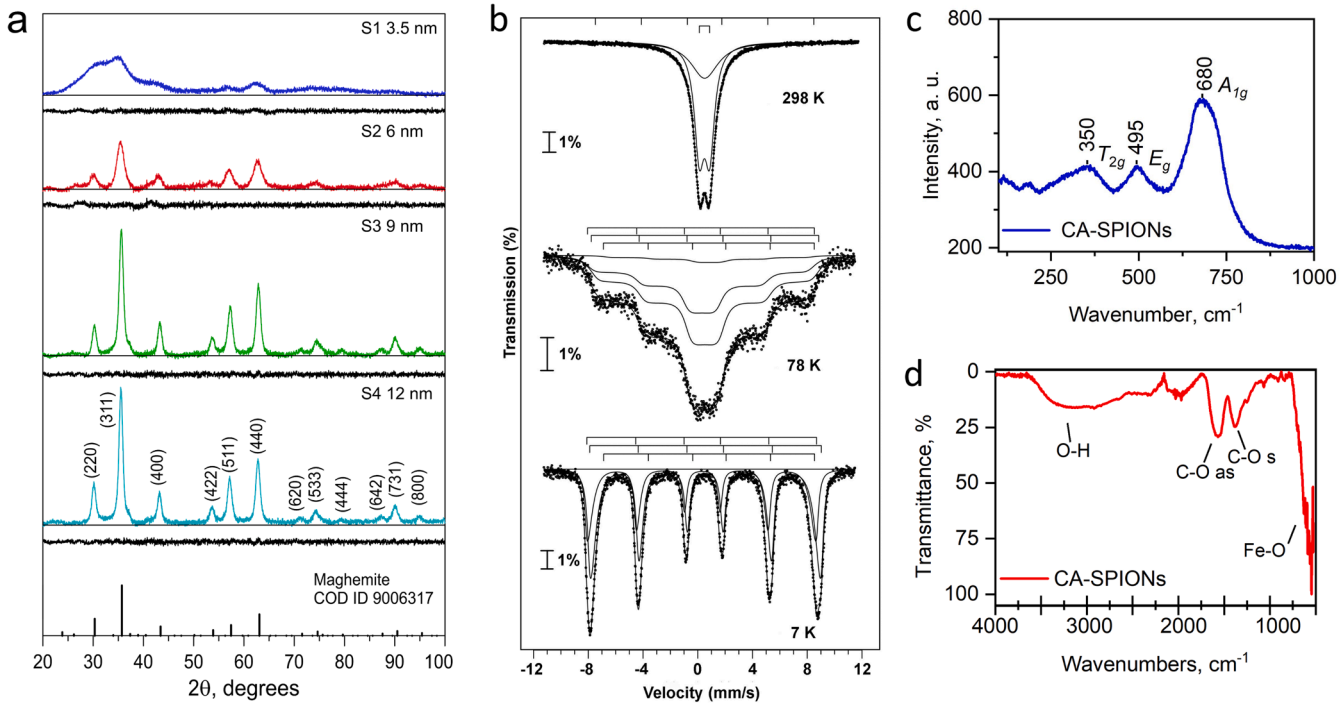

Fig. 2. Structure characterization of CA-SPIONs. a) X-ray powder diffraction pattern for nanoparticles with different core sizes; b) Mössbauer spectra, recorded at 298, 78 и 7 K (open circles) and the resulting curves (solid lines) from the fitting procedure for sample S2; c) Raman spectrum for sample S2; and d) FT-IR spectrum for sample S2.

Fe_3O_4, and maghemite, γ-Fe_2O_3, phases, because their crystal structures are similar. Taking into account the broadening of reflections associated with the nanoscale particles, their X-ray powder diffraction patterns almost completely coincide. Moreover, several modifications of the maghemite crystal structure are known. The cubic structure of the P4132 space group was usually reported (COD ID 9000617) [45]. Maghemite has the structure of a cation-deficient spinel, where the Fe^{3+} ions occur in both tetrahedral and octahedral sites. This crystal structure was used as the starting model for Rietveld analysis. The refinement of structure was stable and gave low R-factors (Table 1, supplementary materials). The average size of the coherent scattering domains (CSD) in the samples of CA-SPIONs was determined by the approximation method from diffraction line broadening using the fundamental parameter (FP) method for the theoretical peak profile calculation. The CSD sizes obtained are consistent with TEM measurements.

The selected-area electron diffraction (SAED) pattern showed polycrystalline diffraction, and the degree of crystallinity increases with increasing the core size (Fig. 1 inserts). The intense diffraction rings can be readily indexed as (220), (311), (400), (422), (511) and (440) in agreement with the XRD data. The presence of large rings with low intensity in the SAED pattern indicates an amorphous phase. Thus, the most amount of amorphous phase is observed in sample S1, while S4 appears to be highly crystalline.

In order to identify the valence state of iron in oxide nanoparticles, Mössbauer spectroscopy was employed (Fig. 2b). The Mössbauer spectra measured at 298, 78 and 7 K show the typical behavior of superparamagnetic nanoparticle assembly [46–50], continuously changing from the broadened superparamagnetic line (298 K) to the magnetic six-line spectrum (7 K) with decreasing temperature. The Mössbauer spectrum of the sample S2 nanoparticles recorded at 298 K consists of a central quadrupole doublet (67 ± 3 %), similar to that of maghemite nanoparticles [46]. We found that the isomer shift and quadrupole splitting to be 0.34 ± 0.01 mm·s^{-1} and 0.75 ± 0.01 mm·s^{-1} respectively, which corresponds to Fe^{3+} ions. The spectrum also shows considerable broadening at the wings of the doublet, and therefore, the relaxation subspectrum (33 ± 3 %) in the model of many-state superparamagnetic relaxation model is introduced in the fit to account for this broadening [51]. This occurred due to the size distribution of the nanoparticles: the superparamagnetic doublet refers to smaller particles, while the broadening is caused by larger ones.

In general, the shape of the relaxation spectrum at a given temperature depends both on the relaxation time τ and on the ratio of the magnetic anisotropy energy to the thermal energy: $\boldsymbol{E_{man}/k_BT}$; the lower the temperature, the greater this ratio and the longer the relaxation time. The spectrum recorded at 78 K shows a very broad, unresolved magnetic component without the paramagnetic one. At 7 K, we already observe a well-defined magnetic sextet pattern with rather narrow resonant lines. These spectra were fitted within the many-state superparamagnetic relaxation model by using three subspectra corresponding to Fe atoms in three different structural-valence states in non-stoichiometric magnetite $Fe_{3-i}O_4$: trivalent Fe^{3+} ions in tetrahedral (A) and octahedral (B) positions – $\mathbf{Fe_A^{3+}}$ and $\mathbf{Fe_B^{3+}}$, and also $Fe^{2.5+}$ ions in the octahedral position – $\mathbf{Fe_B^{2.5+}}$. A detailed description of the spectrum model of $Fe_{3-i}O_4$ nanoparticles taking into account both possible superparamagnetic relaxation and fast electronic exchange between the neighboring $\mathbf{Fe_B^{2+}}$ and $\mathbf{Fe_B^{3+}}$ atoms in the octahedral position was previously presented [52,53]. This model makes it possible to determine not only the hyperfine parameters for magnetite $Fe_{3-i}O_4$ spectrum but also the degree of magnetite nonstoichiometry (*i*), the superparamagnetic relaxation time (τ), the magnetic anisotropy energy (E_{man}) and effective coefficient of uniaxial magnetic anisotropy (K_{eff}) (see details in the supplementary material). The values of the hyperfine parameters of the spectra at 78 and 7 K obtained as a result of model fitting turned out to be close to the corresponding values for maghemite (γ-Fe_2O_3) nanoparticles [47,49]. The obtained values of the degree of non-stoichiometry equal to 0.314 ± 0.12 (at 78 K) and 0.333 ± 0.02 (at 7 K) also indicate that the core of our nanoparticles is composed of almost pure maghemite.

Iron oxide materials are often characterized by vibrational spectroscopy techniques [54–56]. Raman spectra of γ-Fe_2O_3 show distinct signatures in the region 100–1000 cm^{-1}, which allows distinguishing it from other common iron oxide phases including γ-Fe_2O_3 and Fe_3O_4. The spectrum of prepared CA-SPIONs (S2) exhibited all three main Raman shifts at 350, 500, 700 cm^{-1} attributed to T_{2g}, E_g, A_{1g} vibrational modes respectively (Fig. 2c). It was composed of all characteristic peaks for maghemite, and did not contain any peaks associated with magnetite [57,58].

FT-IR spectra of γ-Fe_2O_3 are similar to those of Fe_3O_4 [57,59]; therefore, they are less informative for identifying the phase composition of iron oxide nanoparticles, but they can still be used to additionally characterize adsorbed organic stabilizers. In the FT-IR spectrum of the CA-SPIONs (Fig. 2d) the asymmetric and symmetric stretching vibration of the C=O bond of the citric acid carboxylic groups is located at 1600 and 1400 cm^{-1} respectively. The most intense absorption band in the spectrum at 520–750 cm^{-1} is due to the stretching vibration of the Fe–O bond and the broad absorption at 2400–3500 cm^{-1} can be attributed to the O-H bond of hydroxide groups due to the presence of surface adsorbed water molecules.

To study the elemental composition and valence state of iron in the solid phase of CA-SPIONs XPS was employed. The intense lines of iron, oxygen, and carbon are observed in the survey XPS spectrum (Fig. 3a). The Fe2p photoelectron line is the most informative for the evaluation of the Fe-oxidation state. For all samples, the Fe2p spectra obtained are typical for γ-Fe_2O_3 (Fig. 3b). The same is true for the measured binding energies of the $Fe2p_{3/2}$ (710.7 eV) and $Fe2p_{1/2}$ (724.4 eV) components [60]. Moreover, the satellite located at 718.8 eV in the Fe2p spectra of the samples is observed only for γ-Fe_2O_3, and it is not resolved in the Fe2p spectrum of Fe_3O_4 [61]. Although all the Fe2p spectra are practically the same, there are slight differences observed in the region of 708 eV. The dissimilar intensity of a shoulder in this area is associated with the presence of small but different fractions of Fe^{2+} atoms in the samples.

To determine the proportions of iron atoms in the + 2 and + 3 oxidation states in the samples, the Fe2p spectra were fitted with the synthetic component characteristic of di- and trivalent iron in oxides. The resulting proportions of iron atoms in these oxidation states are shown in Table 1. It can be stated that the Fe^{2+} content in the prepared CA-SPIONs is low and does not exceed 6 %. Thus, based on the combination of applied physicochemical methods, it was confirmed that Fe^{2+} is almost completely oxidized during synthesis and, as a result of the

Table 1
Particle size and composition of the CA-SPIONs.

Parameter	Core size, nm	Hydrodynamic size, nm	ξ-potential, mV	Fe^{II}/Fe ratio		Fe total, mg/mL	
Technique	TEM	DLS	ELS	UV–Vis	XPS	UV–Vis[a]	ICP-MS
S1	3.5 ± 0.7	6 ± 1	−20 ± 1	0.06 ± 0.01	0.06	1.06 ± 0.04	0.98 ± 0.07
S2	6 ± 1	9 ± 1	−25 ± 1	0.04 ± 0.02	0.03	1.22 ± 0.05	1.16 ± 0.06
S3	9 ± 1	17 ± 2	−31 ± 1	0.04 ± 0.02	0.03	1.30 ± 0.10	1.40 ± 0.10
S4	12 ± 2	25 ± 3	−45 ± 1	0.07 ± 0.03	0.05	1.01 ± 0.02	1.00 ± 0.10

[a] The average value of thiocyanate and phenanthroline methods.

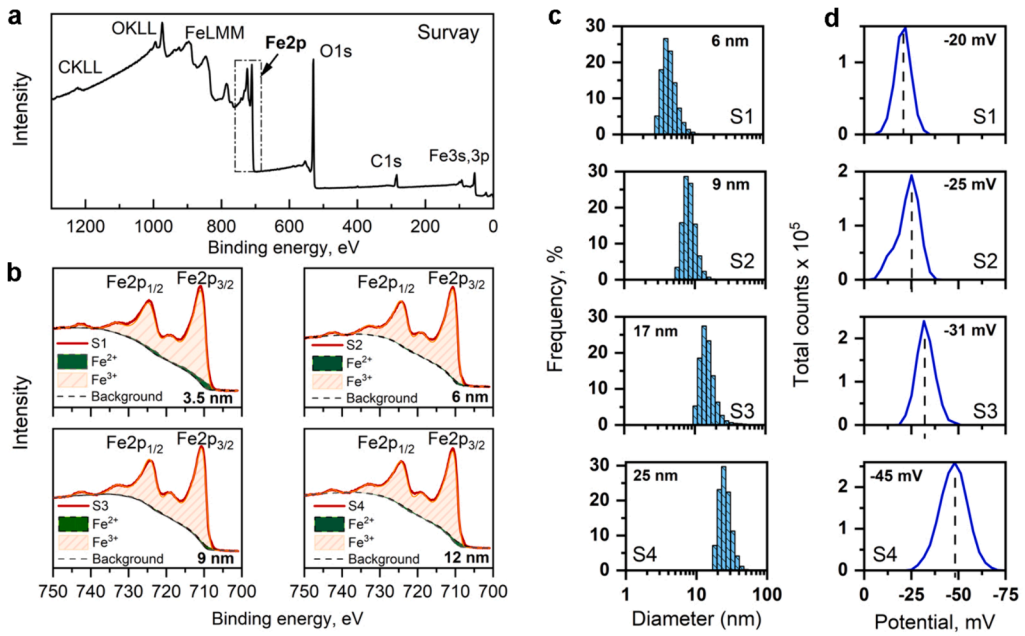

Fig. 3. Elemental composition, valence state of iron in the solid phase and colloidal properties of CA-SPION hydrosol. a) Typical survey and b) Fe2p XPS spectra of CA-SPIONs, c) histogram of the hydrodynamic size distribution measured by DLS and d) zeta-potential measured by ELS.

coprecipitation reaction, maghemite is primarily formed under chosen conditions.

The hydrodynamic size and zeta potential of CA-SPION suspensions was measured by DLS and ELS, respectively. For samples S1-S4 the hydrodynamic size increases incrementally from 6 to 25 nm (Fig. 3c). According to DLS data, no aggregates are formed during synthesis as only one peak can be detected in each sample Furthermore, DLS after a year of storage reveals that the size of CA-SPIONs obtained is stable and does not change (Fig. S3, supplementary materials). The measurements of zeta potential show the characteristic increase of negative potential coupled with increasing the average particle size from −20 mV to −44 mV for S1 and S4, respectively (Fig. 3d), indicating that all samples of prepared CA-SPIONs can be considered as stable aqueous colloids.

Size and composition of iron-oxide nanoparticles strongly influence their magnetic properties. Room-temperature magnetization hysteresis curves display superparamagnetic hysteresis-free behavior for all samples at room temperature (Fig. 4a). The saturation magnetization (M_s) increases with increasing nanoparticle size. M_s value for the smallest 3.5 nm sample (S1) is 2 emu/g whereas M_s for the largest CA-SPIONs of 12 nm (S4) approaches 61 emu/g, which is slightly lower than this value for pure single crystalline bulk maghemite (M_s = 72 emu/g) [62]. A significant decrease in magnetization with decreasing particle diameter was previously observed. Our results correlate with the data published in [63–65]. The relationship between saturation magnetization and nanoparticle size is determined by the ratio of the number of near-surface atoms to the number of atoms in its core. The exchange interaction between magnetic moments on atoms located on the surface is weaker than in the bulk. In particular, partial amorphization of the surface layer of particles leads to changes in exchange interactions. This fact leads to a skew of the magnetic moments on the surface of the particle. The described phenomenon is called canting of magnetic moments [64]. As a result, the saturation magnetization of particles with

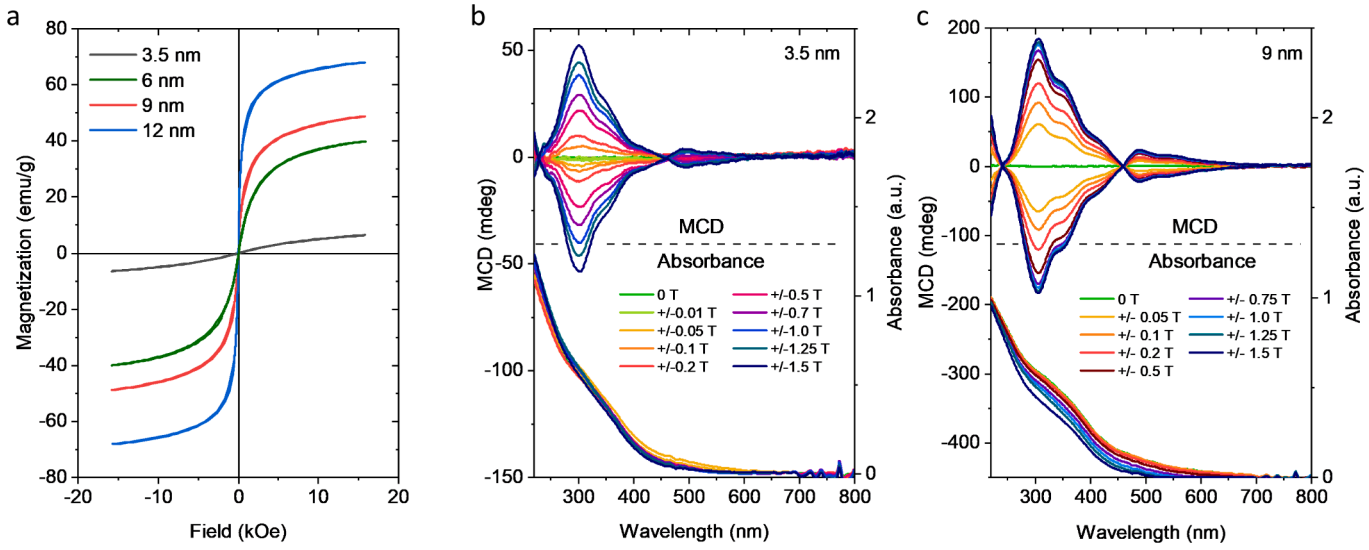

Fig. 4. Magnetization and magnetic field responsive optical properties of CA-SPIONs. a) Magnetization curves at room temperature; b) MCD and absorption spectra of 3.5 nm and c) 9 nm CA-SPIONs at different magnetic field strengths.

small sizes decreases in experiments. We attempted to analyze the behavior of saturation magnetization in maghemite nanoparticles according to the equation [63]:

$$M_s = M_{s0}\left(\frac{\frac{D}{2} - d}{\frac{D}{2}}\right)^3$$

where M_{s0} is the saturation magnetization of pure single crystalline bulk maghemite, D is the particle diameter determined from TEM results, *d* is a magnetically death shell of thickness. According to various estimates, the thickness of the magnetically death shell is approximately 1 nm [63]. The estimated data are presented in Table 2. The obtained results qualitatively coincide with the experimental ones despite the simplicity of the used assessment. Notably, the size of particles where ferromagnetic ordering can be observed is physically limited. Ferromagnetic ordering is impossible at any temperature in particles with a characteristic size of less than 1 nm due to the presence of the Heisenberg uncertainty for the electrons participating in the exchange interaction. Consequently, a further decrease in particle size should lead to the disappearance of saturation magnetization which corresponds with previously published data [63].

An increase in magnetic field inhomogeneities caused by magnetic nanoparticles reduces T_2 relaxation time. In clinical MRI, T_1-weighted and T_2-weighted images are used instead of clear T_1 and T_2 relaxation times. As a result, with significantly reduced T_2 relaxation time, the signal received at short TR (repetition time) and TE (echo time), which corresponds to T_1 weighting, has low intensity. Consequently, an increase in the M_s of nanoparticles leads to a decrease in the signal intensity in the corresponding region in T_1-weighted images. Thus, suppressing the M_s of SPIONs is beneficial for positive contrast agents. Importantly, the effect of T_2 relaxation time on the signal intensity in a T_1-weighted image can be adjusted by changing the TE in the MRI scanner settings.

To investigate the effects of external magnetic field *in situ* on the water colloid of CA-SPIONs with different sizes, we carried out MCD measurements combined with UV–visible spectroscopy for 3.5 and 9 nm nanoparticles. MCD spectroscopy is based on different absorption of light by a substance in a magnetic field with right and left circular polarization. In addition, MCD is able to detect electronic transitions that are too weak to be seen in optical absorption spectra and to distinguish between overlapping transitions.

Fig. 4b,c show the MCD spectra of S1 and S3 at different magnetic field strengths. For both samples the main bands are observed in the region of 250–475 nm and 475–700 nm, which is characteristic of superparamagnetic iron oxides [66]. A complete reversal of the MCD signal is observed in both positive and negative fields, confirming that this is not an experimental artifact [67]. Deconvolution analysis in the range of 250–475 nm revealed three bands with the maxima of 298 nm, 351 nm and 417 nm (Fig. S4a, supplementary materials), which belong to maghemite electronic transitions [68]. Studying the pertinent literature [69,70], we conclude that the decomposition components correspond to transitions from ground state $^6A_1$ to the exited states: $^4T_1$, ^4E and $^4A_1$, for peak 1, peak 2 and peak 3 respectively. Although the hydrosols have equal concentrations, the amplitude of MCD bands for 3.5 nm CA-SPIONs was about four times lower than that of 9 nm, while the absorption was the same. Accordingly, the change of a few nanometers in the core size can be detected using MCD spectroscopy as a trend of increasing signal intensity as the core size increases.

A stepwise increase in the magnetic field strength leads to a gradual increase in the amplitude of the MCD spectra for S1 and at the same time, its absorption does not change significantly even in a high field. On the contrary, for S3 there is a notable decrease in absorption in a field exceeding 0.75 T. It was previously shown that the absorption of free cobalt ferrite particles with a size of 8 nm does not change up to 1.5 T, while the absorption of aggregates of the same particles with a size of 70 nm decreases slightly, and for larger aggregates sedimentation is observed in a field exceeding 0.5 T [71]. Moreover, the dependence of the g-factor of the bands, which is the ratio of the band amplitude MCD-signal to the optical density at the wavelength of the band maximum, in the MCD spectra of magnetic nanoparticles corresponds to the magnetization curve. MCD spectroscopy for SPIONs can therefore be used for qualitative evaluation of magnetic response in aqueous environments. Fig. S4b shows the dependences of the g-factor on the magnetic field with the most intense transition for S1 and S3 samples at 298 nm. For the CA-SPIONs with a core size of 9 nm in the field range from 1.0 to 0.75 T, an S-shaped dependence characteristic of superparamagnetic iron oxide nanoparticles is observed [72]. At high fields from 1.0 to 1.5 T the absorbance decreases, which leads to deviation from the saturation line. The dependence of the g-factor for 3.5 nm CA-SPIONs on the magnetic field strength is linear over the whole range of the applied fields. The observed analysis of g-factor dependence on the magnetic field is in a good agreement with magnetometry measurements. The larger particles show deviations from the characteristic superparamagnetic behavior at high fields, while the small particles demonstrate predominantly a paramagnetic response in aqueous hydrosols over the entire range of fields up to clinical 1.5 T. Thus, the size effect on aggregate formation under an external magnetic field is well controllable. The particles of 3.5 nm remain stable under an applied field of up to 1.5 T, while 9 nm particles tend to aggregate at 1.0 T and above.

Table 2
Magnetic parameters of the CA-SPIONs.

Sample (particle size)	Saturation magnetization, emu/g	Estimated saturation magnetization, emu/g
S1 (3.5 nm)	2 ± 1	6 ± 4
S2 (6 nm)	31 ± 4	22 ± 5
S3 (9 nm)	40 ± 5	35 ± 4
S4 (12 nm)	61 ± 7	43 ± 5

3.2. Iron concentration analysis

The concentration of Fe^{3+}, Fe^{2+} and total Fe in the prepared SPION colloid was measured by UV–Vis spectrophotometry following the thiocyanate and *o*-phenanthroline complexation according to conventional techniques used to study iron in water [73]. The first method based on the interaction of Fe^{2+} with *o*-phenanthroline resulted in the formation of an orange complex with the absorption spectrum maximum at 510 nm. The second one involves Fe^{3+} interaction with the thiocyanate anion forming a red complex with a maximum absorption at 470 nm. The concentration of iron in colloidal solutions of SPIONs can be measured using either of these methods. All details and calibration curves can be found in the supplementary material. The total iron content determined by UV–Vis spectroscopy in stock CA-SPION hydrosols is shown in Table 1. To verify the accuracy of the determined total iron concentration in CA-SPION colloid the ICP-MS was employed. Spectrophotometric data are in good agreement with the values obtained from the ICP-MS reference method, so both thiocyanate and phenanthroline methods are reliable and can be used independently to determine the iron concentration in SPIONs.

The presence of Fe^{3+} ions does not prevent Fe^{2+} determination by the phenanthroline method [74]. This is also true for the thiocyanate method, which determines only Fe^{3+} ions in the presence of Fe^{2+} [75]. Thus, the quantitative assessment of ferrous and ferric iron ions can also be determined by one of these spectrophotometric methods. According to Fe^{2+}/Fe total ratio calculated by UV–Vis spectroscopy the Fe^{2+} content is in the range 4–7 % and this data is very similar to the percentage of Fe^{3+} and Fe^{2+} atomic concentration obtained with quantitative XPS analysis (Table 1). Therefore, spectrophotometry can be used to measure both the concentration and the valency of iron in SPIONs.

3.3. Relaxivity and MRI performance

The prepared magnetic nanoparticles strongly reduce both T_1 and T_2 relaxation times (Table 3). Fig. 5a-e show the $1/T_1$ and $1/T_2$ of all the CA-SPION samples at different concentrations. At iron concentration of 10 mmol/L (0.56 mg/mL) the longitudinal relaxation time (T_1) of pure water is reduced from 3850 to 60, 7 and 4 ms, while transverse relaxation time (T_2) is reduced from 3350 to 41, 4 and 1 ms in the presence of S1, S2 and S3, respectively. S4 showed a strong signal that can be measured even at 0.03 mmol/L (2 μg/mL), where T_1 is 545 ms and T_2 is 115 ms. The r_1 relaxivities of 3.5, 6, 9 and 12 nm CA-SPIONs are 1.64, 14.2, 25 and 36 $L{\cdot}mmol^{-1}{\cdot}s^{-1}$, respectively. The r_2 values also dramatically increase from 2.4 to 230 $L{\cdot}mmol^{-1}{\cdot}s^{-1}$ (Table 3) with the increasing size of nanoparticles from 3.5 to 12 nm.

The best ratio of $r_2/r_1 < 2$ is observed for 3.5 (S1) and 6 nm (S2). The relaxation parameters of 3.5 nm CA-SPIONs are close to commercial Gd-based contrast agents. Even though S1 have a lower r_1 value per paramagnetic metal concentration, 3.5 nm CA-SPIONs should also exhibit intense T_1 contrast due to the low r_2/r_1 ratio. As S2 CA-SPIONs have a higher r_1 than S1, they will have higher T_1 contrast at lower concentrations. For 9 nm (S3) and 12 nm (S4), r_2/r_1 is around 6, which means they will only display T_2 contrast.

Several water-soluble T1 contrast agent formulations of SPIONs with the sizes of 6 nm or less stabilized with small organic ligands were proposed. According to the recent study [76], citrate stabilized SPIONs 3.4 nm in size obtained with microwave-driven synthesis for brain and body angiography exhibited comparable r1 = 1.9 $L{\cdot}mmol^{-1}{\cdot}s^{-1}$ and slightly higher $r_2/r_1 = 2.46$ at 1.5 T. γ-Fe_2O_3 particles coated with a zwitterionic dopamine sulfonate with a core size of 3 nm also showed the same r2/r1 = 2 at 1.5 T [25]. The tannic acid coated maghemite nanoparticles with the size of 3–4 nm developed for T1-enhanced MRI-guided drug delivery showed $r_1 = 2.25\ L{\cdot}mmol^{-1}{\cdot}s^{-1}$ and $r_2/r_1 = 2.34$ at 1.5 T. Interestingly, 5 nm size hydrophobic maghemite nanoparticles obtained through chemical decomposition and transferred using sodium citrate demonstrated similar relaxometry parameters ($r_2/r_1 = 2.46$; $r_1 = 20.76\ L{\cdot}mmol^{-1}{\cdot}s^{-1}$ at 0.5 T) to the obtained S2 nanoparticles with the core size of 6 nm [28]. In general, CA-SPIONs of 3.5 and 6 nm core size have a r_2/r_1 ratio less than 2, suggesting that they are suitable for T1 contrast imaging.

MRI tests were conducted using a 1.5 T clinical MRI scanner to investigate the contrast effect of the prepared nanoparticles. Fig. 5f shows MR images of CA-SPIONs water hydrosols at the iron concentration of 0.01–10 mmol/L (0.6–560 μg/ml). The samples with different concentrations of a contrast agent solution are shown with circles, which are surrounded by deionized water (background). At given settings of MR scanner significant T_1 contrast is observed at the concentrations up to 0.16 mmol/L (9 μg/ml) for S1 and those up to 0.04 mM (2 μg/ml) for S2. In the T_2 weighted images, contrast significantly decreases at the concentrations below 5, 0.63, and 0.08 mM for S1, S2 and S3, respectively. The S4 sample displayed intense negative contrast at a low concentration of 0.01 mmol/L (0.6 μg/ml). For the S4 sample fairly large artifacts (image distortion) were observed in the T_1-WIs at the concentrations higher than 0.63 mmol/L. The contrast is clearly affected by the particle core size. CA-SPIONs with 9 and 12 nm diameters show a high decay of the MR signals in water for T_2- weighted images (T_2-WIs), while T_1 contrast was negligible. In our experiments the S2 sample with an average particle size of 6 nm exhibited T_1 contrast between 0.08 mmol/L (4 μg/ml) and 1.25 mmol/L (0.07 mg/ml). The S_1 with the smallest core size (3.5 nm) revealed the strongest T_1 contrast in the concentration range from 0.31 mmol/L (0.02 mg/ml) to 10 mM (0.56 mg/ml). Compared to the referenced Gd-based contrast agent (Gadovist), the T_1 contrast of S1 appeared at higher concentrations, but had equivalent intensity (Fig. 5g). Gadovist has a T_1-MR signal with the gadolinium concentration of 0.2 to 6.4 mmol/L (0.03 to 1.00 mg/ml) in water solutions.

Table 3
Relaxivities of the CA-SPIONs at 0.47 T.

	r_1, $L{\cdot}mmol^{-1}{\cdot}s^{-1}$	r_2, $L{\cdot}mmol^{-1}{\cdot}s^{-1}$	r_2/r_1
S1	1.64 ± 0.04	2.4 ± 0.1	1.47
S2	14.2 ± 0.9	25 ± 3	1.75
S3	25 ± 2	140 ± 20	5.7
S4	36 ± 5	230 ± 10	5.9
Gadovist	3.5 ± 0.1	4.0 ± 0.2	1.15

Due to high processing T_1 contrast enhancement with 3.5 nm CA-SPIONs, we examined the S1 and Gd samples by MRI in human plasma (Fig. 5h). S1 easily dissolved in plasma forming a slightly colored hydrosol without losing its ability to shorten longitudinal water proton relaxation time. T_2 contrast of CA-SPIONs was clearly seen at the concentrations higher than 0.2 mM (0.01 mg/ml). T_1 contrast was observed in the concentration range from 0.9 to 4.5 mM (0.05–0.25 mg/ml), and artifacts (image distortion) were only observed at high concentrations of 18 mM (1 mg/ml). The results indicate that no aggregates were formed under physiological conditions. The aggregation of SPIONs is usually associated with a drastic decrease in r_1 and an increase in r_2 [77]. The magnetic properties of the colloidal systems are affected by its degree of aggregation: assembling dispersed iron oxide particles results in the magnetic interaction between them, i.e., the magnetic moment ordering and the nanoparticle aggregation. The formation of aggregates is extremely undesirable during MRI, not only due to the increase in r_2 relaxivity [78,79], but also due to the possibility of blocking the blood vessels by micron-sized aggregates after administration [80]. Thus, the absence of aggregation and high T_1 and T_2 contrast suggest that synthesized CA-SPIONs are promising contrast agents for contrast-enhanced MR imaging.

The hydrodynamic size of SPIONs largely determines their biodistribution. SPIONs with a hydrodynamic diameter greater than 20 nm accumulate in the liver and spleen due to macrophage phagocytosis and SPIONs with a hydrodynamic size less than 10 nm are eliminated via the kidneys [81]. Particles with a core size of 3.5 and 6 nm may be partially excreted through the kidneys, while larger particles of 9 and 12 nm are predominantly excreted through the liver. Moreover, the proton relaxation rate strongly depends on the particle size, and the r_2 value is influenced not only by the magnetic particle core radius, but also by its hydrodynamic diameter. The dependence of the r_2 relaxivity on the hydrodynamic radius is well described within classical relaxivity theory. While the core diameter is constant, an increase in the hydrodynamic diameter leads to an increase in the number of water molecules, the diffusion rate of which sufficiently slows down for their dephasing. As a result, an increase in the transverse relaxivity of r_2 is observed. This can be demonstrated with the approved MRI SPIONs – with an increase in the hydrodynamic radius, there is a significant increase in transverse relaxivity with an almost constant value of longitudinal relaxivity and, accordingly, the r_2/r_1 ratio increases. Dextran-stabilized nanoparticles Feridex have a hydrodynamic diameter of 120–180 nm, and their r_1 and r_2 are 10 and 120 $L{\cdot}mmol^{-1}{\cdot}s^{-1}$, respectively. The hydrodynamic diameter of Combidex, which is also stabilized with dextran, is in the range of 15–30 nm, r_2 and r_1 are 10 and 65 $L{\cdot}mmol^{-1}{\cdot}s^{-1}$ respectively [82]. Thus, an increase in the hydrodynamic diameter for the transition from S1 to S4, can also contribute to an increase in the r_2 value.

In MRI, when nanoparticles are administered intravenously, the zeta potential mostly influences the rate of the protein corona formation [83,84]. The surface charge directly depends on the coating material. SPIONs containing carboxyl groups, such as citric acid stabilized S1-S4 samples, have a negative charge. Zeta potential determines the degree of protein adsorption on the nanoparticle surface, and it is directly connected with the blood circulation time of the SPIONs. The blood half-life of citrate-stabilized anion SPIONs is less than 1 h, while for neutral dextran-stabilized nanoparticles, namely Combidex, it is around 24–36 h [82]. Blood proteins cover charged particles faster than the neutral ones. Therefore, the former are easily recognized by macrophages, and

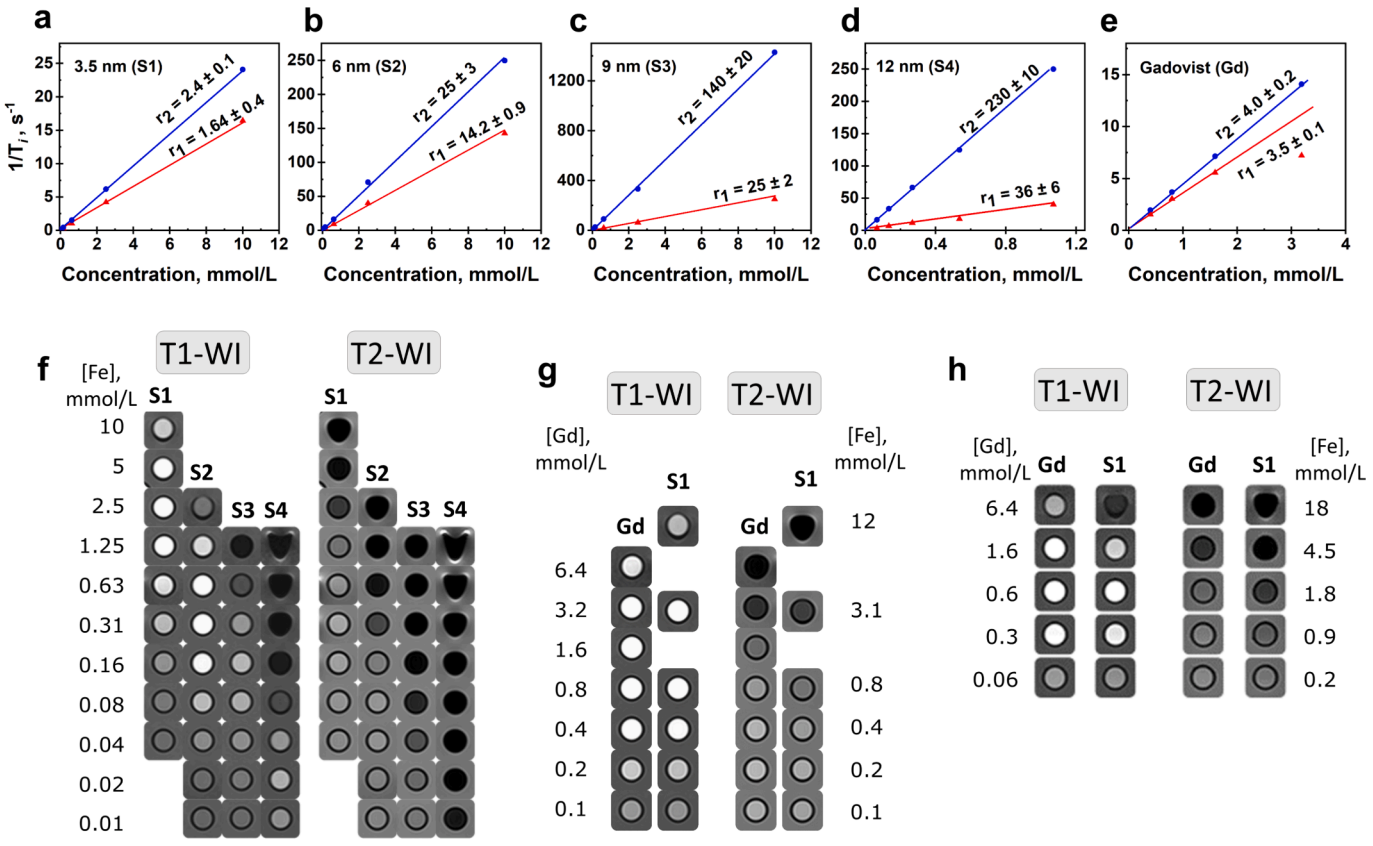

Fig. 5. MR contrast properties of CA-SPIONs. a-e) Relaxivities of water samples as a function of contrast agent concentration at 0.47 T; f,g) MRI images of water and h) human plasma phantoms of CA-SPIONs and Gd-based contrast agent (Gadovist) at different concentrations.

their blood half-life is relatively short, so they tend to accumulate in the liver. But in some cases these properties can be beneficial, since they make citrate-stabilized SPIONs non-toxic and efficient for blood vessel visualization [33].

4. Conclusion

Here we have synthesized the superparamagnetic iron oxide nanoparticles with an average core diameter from 3.5 to 12 nm and PDI≤0.2 using a convenient approach based on a coprecipitation reaction. An automated chemical setup allows for precise control of the synthesis process, resulting in high repeatability and eliminating human error. The CA-SPIONs showed excellent long-term colloidal stability in aqueous media without sedimentation or aggregation. By combining XRD, Mössbauer, Raman and XPS methods to characterize the obtained iron oxide nanoparticles, we have determined that they consist of the primarily maghemite with trace amounts of divalent iron. Moreover, the proposed UV–Vis spectroscopy estimation of total iron concentration and its divalent and trivalent cations separately gives reliable results and can be useful for laboratory testing. From 12 nm to 3.5 nm-sized nanoparticles, saturation magnetization drops sharply from 61 to 2 emu/g. Furthermore, using MCD spectroscopy, we observed signs of aggregate formation *in situ* for 9 nm CA-SPION, but not for 3.5 nm ones at magnetic field up to 1.5 T. According to the obtained relaxivity values and MRI phantom study, these particles are capable of significantly decreasing proton relaxation times at iron concentration range from 10 mmol/L to10 μmol/L depending on the CA-SPION size and preferable MRI modality. In our study, we varied only the magnetic core size as a measure of relaxation enhancement, and although the coating remained consistent, the electrostatic layer contribution in overall hydrodynamic size also increased with the increasing core size. The increasing core size collectively enhanced the r_2 and r_1 relaxivity, but to a different extent, which led to a signal suppression on T_1-WIs and to a strong contrast effect on T_2-WIs. Therefore, small-sized SPIONs are likely to be T_1 dominated contrast agents, with reduced r_2 relaxivity. In water and blood plasma, 3.5 nm particles possess a strong T_1 contrast at a concentration slightly higher than that of commercial Gd-based contrast agent (Gadovist). SPIONs at the size less than 6 nm exhibit the r_2/r_1 ratio below 2. Finally, we carried out a complex study of the chemical composition and structure of iron oxide nanoparticles and obtained valuable information for developing next generation iron oxide nanoparticle-based MRI contrast agents.

Author contributions

All authors equally contributed to writing of the manuscript and approved the final version. These authors contributed equally.

CRediT authorship contribution statement

Ekaterina O. Moiseeva: Writing – review & editing, Writing – original draft, Visualization, Methodology, Investigation, Formal analysis, Data curation, Conceptualization. **Sergei V. German:** Writing – review & editing, Conceptualization, Formal analysis, Visualization. **Aleksei S. Komlev:** Writing – review & editing, Writing – original draft, Methodology, Investigation, Formal analysis, Data curation. **Vyacheslav S. Rusakov:** Writing – review & editing, Writing – original draft, Methodology, Investigation, Formal analysis, Data curation. **Viktor V. Zuev:** Investigation, Data curation. **Olga S. Pavlova:** Writing – review & editing, Writing – original draft, Visualization, Methodology, Investigation, Funding acquisition, Formal analysis, Data curation. **Alexander M. Perepukhov:** Writing – review & editing, Methodology, Investigation, Formal analysis, Data curation. **Artem O. Dmitrienko:** Writing – review & editing, Investigation, Formal analysis, Data curation.

Konstantin I. Maslakov: Writing – review & editing, Formal analysis, Data curation. **Olga Y. Griaznova:** Writing – review & editing, Formal analysis, Data curation. **Alexander V. Finko:** Writing – review & editing, Formal analysis, Data curation. **Antonina I. Dadadzhanova:** Writing – review & editing, Writing – original draft, Visualization, Formal analysis, Data curation, Conceptualization. **Vasiliy S. Chernyshev:** Writing – review & editing, Writing – original draft, Visualization, Formal analysis, Data curation. **Anna O. Orlova:** Writing – review & editing, Funding acquisition, Formal analysis, Methodology. **Dmitry A. Gorin:** Writing – review & editing, Supervision, Project administration, Funding acquisition, Conceptualization.

Declaration of competing interest

The authors declare that they have no known competing financial interests or personal relationships that could have appeared to influence the work reported in this paper.

Data availability

Data will be made available on request.

Acknowledgment

This work was supported by Clover Program: Joint Research Projects of Skoltech, MIPT, and ITMO. Magnetic properties measurements were supported by Russian Ministry of Science and Education grant No. 075-15-2021-1353. The authors acknowledge the support from Lomonosov Moscow State University Program of Development for providing access to the XPS facility. The authors are grateful to the AICF of Skoltech for providing access to the TEM facilities and Maria Kirsanova for microscope operation.

Appendix A. Supplementary data

Supplementary data to this article can be found online at https://doi.org/10.1016/j.jmmm.2024.172447.

References

[1] G.J. Strijkers, W.J. M Mulder, G.A. F van Tilborg, K. Nicolay, MRI contrast agents: current status and future perspectives, Anti-Cancer Agents in Medicinal Chemistry (Formerly Current Medicinal Chemistry-Anti-Cancer Agents), 7 (2007) 291-305, Doi: 10.2174/187152007780618135.
[2] C. Westbrook, J. Talbot, MRI in Practice, John Wiley & Sons, 2018.
[3] M.T. Vlaardingerbroek, J.A. Boer, Magnetic resonance imaging: theory and practice, Springer Science & Business Media, 2013.
[4] J. Wahsner, E.M. Gale, A. Rodríguez-Rodríguez, P. Caravan, Chemistry of MRI contrast agents: current challenges and new frontiers, Chem. Rev. 119 (2018) 957–1057, https://doi.org/10.1021/acs.chemrev.8b00363.
[5] A. Frtús, B. Smolková, M. Uzhytchak, M. Lunova, M. Jirsa, Š. Kubinová, A. Dejneka, O. Lunov, Analyzing the mechanisms of iron oxide nanoparticles interactions with cells: a road from failure to success in clinical applications, J. Control. Release 328 (2020) 59–77, https://doi.org/10.1016/j.jconrel.2020.08.036.
[6] H.B. Na, I.C. Song, T. Hyeon, Inorganic nanoparticles for MRI contrast agents, Adv. Mater. 21 (2009) 2133–2148, https://doi.org/10.1002/adma.200802366.
[7] C.L. Bennett, Z.P. Qureshi, A.O. Sartor, L.B. Norris, A. Murday, S. Xirasagar, H. S. Thomsen, Gadolinium-induced nephrogenic systemic fibrosis: the rise and fall of an iatrogenic disease, Clin. Kidney J. 5 (2012) 82–88, https://doi.org/10.1093/ckj/sfr172.
[8] J. Heverhagen, G. Krombach, E. Gizewski, Application of extracellular gadolinium-based MRI contrast agents and the risk of nephrogenic systemic fibrosis, RöFo-Fortschritte auf dem Gebiet der Röntgenstrahlen und der bildgebenden Verfahren, © Georg Thieme Verlag KG (2014) 661–669, https://doi.org/10.1055/s-0033-1356403.
[9] I. Krefting, Gadolinium retention following gadolinium based contrast agent MRIs: brain and other organs. September 8, 2017 Meeting of the Medical Imaging Drugs Advisory Committee (MIDAC): US Food and Drug Administration, 2017.
[10] W. Li, S. Tutton, A.T. Vu, L. Pierchala, B.S. Li, J.M. Lewis, P.V. Prasad, R. R. Edelman, First-pass contrast-enhanced magnetic resonance angiography in humans using ferumoxytol, a novel ultrasmall superparamagnetic iron oxide (USPIO)-based blood pool agent, J. Magnet. Reson. Imag. Off. J. Int. Soc. Magn. Reson. Med. 21 (2005) 46–52, https://doi.org/10.1002/jmri.20235.
[11] T. Shen, R. Weissleder, M. Papisov, A. Bogdanov Jr, T.J. Brady, Monocrystalline iron oxide nanocompounds (MION): physicochemical properties, Magn. Reson. Med. 29 (1993) 599–604, https://doi.org/10.1002/mrm.1910290504.
[12] B.H. Kim, N. Lee, H. Kim, K. An, Y.I. Park, Y. Choi, K. Shin, Y. Lee, S.G. Kwon, H. B. Na, Large-scale synthesis of uniform and extremely small-sized iron oxide nanoparticles for high-resolution T 1 magnetic resonance imaging contrast agents, J. Am. Chem. Soc. 133 (2011) 12624–12631, https://doi.org/10.1021/ja203340u.
[13] U.I. Tromsdorf, O.T. Bruns, S.C. Salmen, U. Beisiegel, H. Weller, A highly effective, nontoxic T 1 MR contrast agent based on ultrasmall PEGylated iron oxide nanoparticles, Nano Lett. 9 (2009) 4434–4440, https://doi.org/10.1021/nl902715v.
[14] D. Shrivastava, J.T. Vaughan, Safety and Biological Effects in MRI, John Wiley & Sons, 2020.
[15] H. Arami, A. Khandhar, D. Liggitt, K.M. Krishnan, In vivo delivery, pharmacokinetics, biodistribution and toxicity of iron oxide nanoparticles, Chem. Soc. Rev. 44 (2015) 8576–8607, https://doi.org/10.1039/c5cs00541h.
[16] E. Rahimi, R. Sanchis-Gual, X. Chen, A. Imani, Y. Gonzalez-Garcia, E. Asselin, A. Mol, L. Fedrizzi, S. Pané, M. Lekka, Challenges and strategies for optimizing corrosion and biodegradation stability of biomedical micro-and nanoswimmers: a review, Adv. Funct. Mater. 33 (2023) 2210345, https://doi.org/10.1002/adfm.202210345.
[17] H. Etemadi, J.K. Buchanan, N.G. Kandile, P.G. Plieger, Iron oxide nanoparticles: Physicochemical characteristics and historical developments to commercialization for potential technological applications, ACS Biomater Sci. Eng. 7 (2021) 5432–5450, https://doi.org/10.1021/acsbiomaterials.1c00938.
[18] A.S. Fortuin, R. Brüggemann, J. van der Linden, I. Panfilov, B. Israël, T. W. Scheenen, J.O. Barentsz, Ultra-small superparamagnetic iron oxides for metastatic lymph node detection: Back on the block, Wiley Interdiscip. Rev. Nanomed. Nanobiotechnol. 10 (2018) e1471.
[19] Y.-X. Wang, Current status of superparamagnetic iron oxide contrast agents for liver magnetic resonance imaging, World J. Gastroenterol. 21 (2015) 13400–13402, https://doi.org/10.3748/wjg.v21.i47.13400.
[20] G.B. Toth, C.G. Varallyay, A. Horvath, M.R. Bashir, P.L. Choyke, H.E. Daldrup-Link, E. Dosa, J.P. Finn, S. Gahramanov, M. Harisinghani, Current and potential imaging applications of ferumoxytol for magnetic resonance imaging, Kidney Int. 92 (2017) 47–66, https://doi.org/10.1016/j.kint.2016.12.037.
[21] B.J. McCullough, O. Kolokythas, J.H. Maki, D.E. Green, Ferumoxytol in clinical practice: implications for MRI, J. Magn. Reson. Imaging 37 (2013) 1476–1479, https://doi.org/10.1002/jmri.23879.
[22] S. Alzola-Aldamizetxebarria, L. Fernández-Méndez, D. Padro, J. Ruíz-Cabello, P. Ramos-Cabrer, A comprehensive introduction to magnetic resonance imaging relaxometry and contrast agents, ACS Omega 7 (2022) 36905–36917, https://doi.org/10.1021/acsomega.2c03549.
[23] M. Jeon, M.V. Halbert, Z.R. Stephen, M. Zhang, Iron oxide nanoparticles as T1 contrast agents for magnetic resonance imaging: fundamentals, challenges, applications, and prospectives, Adv. Mater. 33 (2021) 1906539, https://doi.org/10.1002/adma.201906539.
[24] D. Liu, W. Wu, J. Ling, S. Wen, N. Gu, X. Zhang, Effective PEGylation of iron oxide nanoparticles for high performance in vivo cancer imaging, Adv. Funct. Mater. 21 (2011) 1498–1504, https://doi.org/10.1002/adfm.201001658.
[25] H. Wei, O.T. Bruns, M.G. Kaul, E.C. Hansen, M. Barch, A. Wiśniowska, O. Chen, Y. Chen, N. Li, S. Okada, Exceedingly small iron oxide nanoparticles as positive MRI contrast agents, Proc. Natl. Acad. Sci. 114 (2017) 2325–2330, https://doi.org/10.1073/pnas.1620145114.
[26] F. Hu, Q. Jia, Y. Li, M. Gao, Facile synthesis of ultrasmall PEGylated iron oxide nanoparticles for dual-contrast T1-and T2-weighted magnetic resonance imaging, Nanotechnology 22 (2011) 245604, https://doi.org/10.1088/0957-4484/22/24/245604.
[27] T. Vangijzegem, D. Stanicki, S. Boutry, Q. Paternoster, L. Vander Elst, R. Muller, S. Laurent, VSION as high field MRI T1 contrast agent: Evidence of their potential as positive contrast agent for magnetic resonance angiography, Nanotechnology, 29 (2018) 265103, Doi: 10.1088/1361-6528/aabbd0.
[28] E. Taboada, E. Rodríguez, A. Roig, J. Oró, A. Roch, R.N. Muller, Relaxometric and magnetic characterization of ultrasmall iron oxide nanoparticles with high magnetization. Evaluation as potential T 1 magnetic resonance imaging contrast agents for molecular imaging, Langmuir 23 (2007) 4583–4588, https://doi.org/10.1021/la063415s.
[29] Z. Li, P.W. Yi, Q. Sun, H. Lei, H. Li Zhao, Z.H. Zhu, S.C. Smith, M.B. Lan, G.Q. Lu, Ultrasmall water-soluble and biocompatible magnetic iron oxide nanoparticles as positive and negative dual contrast agents, Adv. Funct. Mater. 22 (2012) 2387–2393, https://doi.org/10.1002/adfm.201103123.
[30] E.-J. Park, H.N. Umh, D.-H. Choi, M.H. Cho, W. Choi, S.-W. Kim, Y. Kim, J.-H. Kim, Magnetite-and maghemite-induced different toxicity in murine alveolar macrophage cells, Arch. Toxicol. 88 (2014) 1607–1618, https://doi.org/10.1007/s00204-014-1210-1.
[31] H. Shokrollahi, A review of the magnetic properties, synthesis methods and applications of maghemite, J. Magn. Magn. Mater. 426 (2017) 74–81, https://doi.org/10.1016/j.jmmm.2016.11.033.
[32] M. Barrow, A. Taylor, A.M. Fuentes-Caparrós, J. Sharkey, L.M. Daniels, P. Mandal, B.K. Park, P. Murray, M.J. Rosseinsky, D.J. Adams, SPIONs for cell labelling and tracking using MRI: magnetite or maghemite? Biomater. Sci. 6 (2018) 101–106, https://doi.org/10.1039/c7bm00515f.
[33] M. Taupitz, S. Wagner, J. Schnorr, Phase I clinical evaluation of citrate-coated monocrystalline very small superparamagnetic iron oxide particles as a new contrast medium for magnetic resonance imaging.(vol 39, pg 394, 2004),

Investigat. Radiol., 39 (2004) 625-625, Doi: 10.1097/01.rli.0000129472.45832.b0.
[34] J. Schnorr, M. Taupitz, E. Schellenberger, C. Warmuth, U. Fahlenkamp, S. Wagner, N. Kaufels, M. Wagner, Cardiac magnetic resonance angiography using blood-pool contrast agents: comparison of citrate-coated very small superparamagnetic iron oxide particles with gadofosveset trisodium in pigs, in: Röfo-Fortschritte Auf Dem Gebiet Der Röntgenstrahlen Und Der Bildgebenden Verfahren, © Georg Thieme Verlag KG, 2012, pp. 105–112, https://doi.org/10.1055/s-0031-1281982.
[35] J. Schnorr, S. Wagner, C. Abramjuk, I. Wojner, T. Schink, T.J. Kroencke, E. Schellenberger, B. Hamm, H. Pilgrimm, M. Taupitz, Comparison of the iron oxide-based blood-pool contrast medium VSOP-C184 with gadopentetate dimeglumine for first-pass magnetic resonance angiography of the aorta and renal arteries in pigs, Invest. Radiol. 39 (2004) 546–553, https://doi.org/10.1097/01.rli.0000133944.30119.cc.
[36] E. Tysiak, P. Asbach, O. Aktas, H. Waiczies, M. Smyth, J. Schnorr, M. Taupitz, J. Wuerfel, Beyond blood brain barrier breakdown–in vivodetection of occult neuroinflammatory foci by magnetic nanoparticles in high field MRI, J. Neuroinflammation 6 (2009) 1–8, https://doi.org/10.1186/1742-2094-6-20.
[37] R. Massart, Preparation of aqueous magnetic liquids in alkaline and acidic media, IEEE Trans. Magn. 17 (1981) 1247–1248, https://doi.org/10.1109/TMAG.1981.1061188.
[38] M. Matsnev, V. Rusakov, SpectrRelax: An application for Mössbauer spectra modeling and fitting, in: AIP Conference Proceedings, American Institute of Physics, 2012, pp. 178–185, https://doi.org/10.1063/1.4759488.
[39] C.-R. Lin, R.-K. Chiang, J.-S. Wang, T.-W. Sung, Magnetic properties of monodisperse iron oxide nanoparticles, J. Appl. Phys. 99 (2006) 08N710, https://doi.org/10.1063/1.2172891.
[40] S. German, O. Inozemtseva, A. Markin, K. Metvalli, G. Khomutov, D. Gorin, Synthesis of magnetite hydrosols in inert atmosphere, Colloid J. 75 (2013) 483–486, https://doi.org/10.1134/S1061933X13040042.
[41] N. Gribanov, E. Bibik, O. Buzunov, V. Naumov, Physico-chemical regularities of obtaining highly dispersed magnetite by the method of chemical condensation, J. Magn. Magn. Mater. 85 (1990) 7–10, https://doi.org/10.1016/0304-8853(90)90005-B.
[42] L. Vayssieres, C. Chanéac, E. Tronc, J.P. Jolivet, Size tailoring of magnetite particles formed by aqueous precipitation: an example of thermodynamic stability of nanometric oxide particles, J. Colloid Interface Sci. 205 (1998) 205–212, https://doi.org/10.1006/jcis.1998.5614.
[43] J. Park, K. An, Y. Hwang, J.-G. Park, H.-J. Noh, J.-Y. Kim, J.-H. Park, N.-M. Hwang, T. Hyeon, Ultra-large-scale syntheses of monodisperse nanocrystals, Nat. Mater. 3 (2004) 891–895, https://doi.org/10.1038/nmat1251.
[44] Z. Zhou, L. Yang, J. Gao, X. Chen, Structure–relaxivity relationships of magnetic nanoparticles for magnetic resonance imaging, Adv. Mater. 31 (2019) 1804567, https://doi.org/10.1002/adma.201804567.
[45] C. Pecharromán, T. Gonzalez-Carreno, J.E. Iglesias, The infrared dielectric properties of maghemite, γ-Fe_2O_3, from reflectance measurement on pressed powders, Phys. Chem. Miner. 22 (1995) 21–29, https://doi.org/10.1007/BF00202677.
[46] E. Tronc, A. Ezzir, R. Cherkaoui, C. Chanéac, M. Noguès, H. Kachkachi, D. Fiorani, A. Testa, J. Greneche, J. Jolivet, Surface-related properties of γ-Fe_2O_3 nanoparticles, J. Magn. Magn. Mater. 221 (2000) 63–79, https://doi.org/10.1016/S0304-8853(00)00369-3.
[47] A.G. Roca, J.F. Marco, M.d.P. Morales, C.J. Serna, Effect of nature and particle size on properties of uniform magnetite and maghemite nanoparticles, J. Phys. Chem. C 111 (2007) 18577–18584, https://doi.org/10.1021/jp075133m.
[48] L. Häggström, S. Kamali, T. Ericsson, P. Nordblad, A. Ahniyaz, L. Bergström, Mössbauer and magnetization studies of iron oxide nanocrystals, Hyperfine Interact. 183 (2008) 49–53, https://doi.org/10.1007/s10751-008-9750-5.
[49] J. Ramos Guivar, A. Bustamante, J. Flores, M. Mejía Santillan, A. Osorio, A. Martínez, L. De Los Santos, C.B. Valladares, Mössbauer study of intermediate superparamagnetic relaxation of maghemite (γ-Fe_2O_3) nanoparticles, Hyperfine Interact. 224 (2014) 89–97, https://doi.org/10.1007/s10751-013-0864-z.
[50] H. Hah, A. Williams, W. Pham, C. Johnson, J. Johnson, Magnetic properties of the MRI enhancement agent Feridex from Mössbauer spectra, Hyperfine Interact. 242 (2021) 1–5, https://doi.org/10.1007/s10751-021-01739-1.
[51] D. Jones, K. Srivastava, Many-state relaxation model for the Mössbauer spectra of superparamagnets, Phys. Rev. B 34 (1986) 7542, https://doi.org/10.1103/PhysRevB.34.7542.
[52] M. Fadeev, A. Kozlovskiy, I. Korolkov, K. Egizbek, A. Nazarova, D. Chudoba, V. Rusakov, M. Zdorovets, Iron oxide@ gold nanoparticles: Synthesis, properties and potential use as anode materials for lithium-ion batteries, Colloids Surf. A Physicochem. Eng. Asp. 603 (2020) 125178, https://doi.org/10.1016/j.colsurfa.2020.125178.
[53] I. Korolkov, K. Ludzik, A. Kozlovskiy, M. Fadeev, A. Shumskaya, Y.G. Gorin, M. Jazdzewska, M. Anisovich, V. Rusakov, M. Zdorovets, Immobilization of carboranes on Fe_3O_4-polymer nanocomposites for potential application in boron neutron cancer therapy, Colloids Surf. A Physicochem. Eng. Asp. 601 (2020) 125035, https://doi.org/10.1016/j.colsurfa.2020.125035.
[54] I. Chernyshova, M. Hochella Jr, A. Madden, Size-dependent structural transformations of hematite nanoparticles. 1. Phase transition, PCCP 9 (2007) 1736–1750, https://doi.org/10.1039/B618790K.
[55] A.C. Moreno Maldonado, E.L. Winkler, M. Raineri, A. Toro Córdova, L. M. Rodríguez, H.E. Troiani, M.L. Mojica Pisciotti, M.V. Mansilla, D. Tobia, M. S. Nadal, Free-radical formation by the peroxidase-like catalytic activity of MFe2O4 (M= Fe, Ni, and Mn) nanoparticles, J. Phys. Chem. C 123 (2019) 20617–20627, https://doi.org/10.1021/acs.jpcc.9b05371.
[56] J. Mürbe, A. Rechtenbach, J. Töpfer, Synthesis and physical characterization of magnetite nanoparticles for biomedical applications, Mater. Chem. Phys. 110 (2008) 426–433, https://doi.org/10.1016/j.matchemphys.2008.02.037.
[57] A.M. Jubb, H.C. Allen, Vibrational spectroscopic characterization of hematite, maghemite, and magnetite thin films produced by vapor deposition, ACS Appl. Mater. Interfaces 2 (2010) 2804–2812, https://doi.org/10.1021/am1004943.
[58] L.B. Salviano, T.M.d.S. Cardoso, G.C. Silva, M.S.S. Dantas, A.d.M. Ferreira, Microstructural assessment of magnetite nanoparticles (Fe_3O_4) obtained by chemical precipitation under different synthesis conditions, Mater. Res. 21 (2018), https://doi.org/10.1590/1980-5373-MR-2017-0764.
[59] M. Aliahmad, N. Nasiri Moghaddam, Synthesis of maghemite (γ-Fe_2O_3) nanoparticles by thermal-decomposition of magnetite (Fe_3O_4) nanoparticles, Mater. Sci.-Pol. 31 (2013) 264–268, https://doi.org/10.2478/s13536-012-0100-6.
[60] T. Yamashita, P. Hayes, Analysis of XPS spectra of Fe^{2+} and Fe^{3+} ions in oxide materials, Appl. Surf. Sci. 254 (2008) 2441–2449, https://doi.org/10.1016/j.apsusc.2007.09.063.
[61] S. Gota, E. Guiot, M. Henriot, M. Gautier-Soyer, Atomic-oxygen-assisted MBE growth of α-Fe_2O_3 on α-Al_2O_3 (0001): Metastable FeO (111)-like phase at subnanometer thicknesses, Phys. Rev. B 60 (1999) 14387, https://doi.org/10.1103/PhysRevB.60.14387.
[62] S.P. Gubin, Magnetic nanoparticles, John Wiley & Sons, 2009.
[63] A. Millan, A. Urtizberea, N. Silva, F. Palacio, V. Amaral, E. Snoeck, V. Serin, Surface effects in maghemite nanoparticles, J. Magn. Magn. Mater. 312 (2007) L5–L9, https://doi.org/10.1016/j.jmmm.2006.09.011.
[64] M.P. Morales, S. Veintemillas-Verdaguer, M. Montero, C. Serna, A. Roig, L. Casas, B. Martinez, F. Sandiumenge, Surface and internal spin canting in γ-Fe_2O_3 nanoparticles, Chem. Mater. 11 (1999) 3058–3064, https://doi.org/10.1021/cm991018f.
[65] V. Nikiforov, A. Goldt, E. Gudilin, V. Sredin, V.Y. Irhin, Magnetic properties of maghemite nanoparticles, Bull. Russ. Acad. Sci. Phys. 78 (2014) 1075–1080, https://doi.org/10.3103/S1062873814100141.
[66] G. Campo, F. Pineider, V. Bonanni, M. Albino, A. Caneschi, C. de Julián Fernández, C. Innocenti, C. Sangregorio, Magneto-optical probe for investigation of multiphase Fe oxide nanosystems, Chem. Mater. 27 (2015) 466–473, https://doi.org/10.1021/cm5034595.
[67] H. Yao, Y. Ishikawa, Finite size effect on magneto-optical responses of chemically modified Fe_3O_4 nanoparticles studied by MCD spectroscopy, J. Phys. Chem. C 119 (2015) 13224–13230, https://doi.org/10.1021/acs.jpcc.5b03131.
[68] E. Fantechi, G. Campo, D. Carta, A. Corrias, C. de Julián Fernández, D. Gatteschi, C. Innocenti, F. Pineider, F. Rugi, C. Sangregorio, Exploring the effect of Co doping in fine maghemite nanoparticles, J. Phys. Chem. C 116 (2012) 8261–8270, https://doi.org/10.1021/jp300806j.
[69] R.M. Cornell, U. Schwertmann, The iron oxides: structure, properties, reactions, occurrences, and uses, Wiley-vch Weinheim, 2003, Doi: 10.1515/CORRREV.1997.15.3-4.533.
[70] R.V. Morris, H.V. Lauer Jr, C.A. Lawson, E.K. Gibson Jr, G.A. Nace, C. Stewart, Spectral and other physicochemical properties of submicron powders of hematite (α-Fe_2O_3), maghemite (γ-Fe_2O_3), magnetite (Fe3O4), goethite (α-FeOOH), and lepidocrocite (γ-FeOOH), J. Geophys. Res. Solid Earth 90 (1985) 3126–3144, https://doi.org/10.1029/JB090iB04p03126.
[71] Y.A. Gromova, V.G. Maslov, M.A. Baranov, R. Serrano-García, V.A. Kuznetsova, F. Purcell-Milton, Y.K. Gun'ko, A.V. Baranov, A.V. Fedorov, Magnetic and optical properties of isolated and aggregated $CoFe_2O_4$ superparamagnetic nanoparticles studied by MCD spectroscopy, J. Phys. Chem. C 122 (2018) 11491–11497, https://doi.org/10.1021/acs.jpcc.8b00829.
[72] A. Matiushkina, A. Bazhenova, I. Litvinov, T. Belyaeva, E. Kornilova, A. Dubavik, A. Orlova, Magneto-luminescent nanostructures for biomedicine, J. Physi.: Conf. Series, IOP Publishing, 2021, pp. 012003, Doi: 10.1088/1742-6596/1866/1/012003.
[73] A. Reznikov, E. Mulikovskaya, I.Y. Sokolov, Methods of Water Analysis, 285, Nedra, Moscow, 1970.
[74] L. Herrera, P. Ruiz, J.C. Aguillon, A. Fehrmann, A new spectrophotometric method for the determination of ferrous iron in the presence of ferric iron, J. Chem. Technol. Biotechnol. 44 (1989) 171–181, https://doi.org/10.1002/jctb.280440302.
[75] F. Martins, J. Andrade, A. Pimenta, L. Lourenço, J. Castro, V. Balbo, Estudo espectrofotométrico da oxidação de ferro no sistema ferro (II)/tiocianato/acetona e algumas aplicações analíticas, Eclética Química 30 (2005) 63–71, https://doi.org/10.1590/S0100-46702005000300008.
[76] J. Pellico, J.s. Ruiz-Cabello, I. Fernández-Barahona, L. Gutierrez, A.V. Lechuga-Vieco, J.A. Enríquez, M.P. Morales, F. Herranz, One-step fast synthesis of nanoparticles for MRI: coating chemistry as the key variable determining positive or negative contrast, Langmuir 33 (2017) 10239–10247, https://doi.org/10.1021/acs.langmuir.7b01759.
[77] A. Roch, Y. Gossuin, R.N. Muller, P. Gillis, Superparamagnetic colloid suspensions: water magnetic relaxation and clustering, J. Magnet. Magnet. Mater. 293 (2005) 532–539, https://doi.org/10.1016/j.jmmm.2005.01.070.
[78] M. Tadic, J. Lazovic, M. Panjan, S. Kralj, Hierarchical iron oxide nanocomposite: Bundle-like morphology, magnetic properties and potential biomedical application, Ceram. Int. 48 (2022) 16015–16022, https://doi.org/10.1016/j.ceramint.2022.02.145.
[79] M. Tadic, S. Kralj, M. Jagodic, D. Hanzel, D. Makovec, Magnetic properties of novel superparamagnetic iron oxide nanoclusters and their peculiarity under annealing treatment, Appl. Surf. Sci. 322 (2014) 255–264, https://doi.org/10.1016/j.apsusc.2014.09.181.

[80] P. Vartholomeos, C. Mavroidis, Simulation platform for self-assembly structures in MRI-guided nanorobotic drug delivery systems, 2010 IEEE International Conference on Robotics and Automation, IEEE, 2010, pp. 5594-5600, Doi: 10.1109/ROBOT.2010.5509711.
[81] J. Dolai, K. Mandal, N.R. Jana, Nanoparticle size effects in biomedical applications, ACS Appl. Nano Mater. 4 (2021) 6471–6496, https://doi.org/10.1021/acsanm.1c00987.
[82] M.M. Modo, J.W. Bulte, Molecular and cellular MR imaging, CRC Press, 2007.
[83] C.D. Walkey, W.C. Chan, Understanding and controlling the interaction of nanomaterials with proteins in a physiological environment, Chem. Soc. Rev. 41 (2012) 2780–2799, https://doi.org/10.1039/c1cs15233e.
[84] M. Colombo, L. Fiandra, G. Alessio, S. Mazzucchelli, M. Nebuloni, C. De Palma, K. Kantner, B. Pelaz, R. Rotem, F. Corsi, Tumour homing and therapeutic effect of colloidal nanoparticles depend on the number of attached antibodies, Nat. Commun. 7 (2016) 13818, https://doi.org/10.1038/ncomms13818.